Modeling the Influence of the Weddell Polynya on the Filchner–Ronne Ice Shelf Cavity

KAITLIN A. NAUGHTEN, ADRIAN JENKINS, PAUL R. HOLLAND, RUTH I. MUGFORD, KEITH W. NICHOLLS, AND DAVID R. MUNDAY

British Antarctic Survey, Cambridge, United Kingdom

(Manuscript received 13 March 2019, in final form 21 May 2019)

ABSTRACT

Open-ocean polynyas in the Weddell Sea of Antarctica are the product of deep convection, which transports Warm Deep Water (WDW) to the surface and melts sea ice or prevents its formation. These polynyas occur only rarely in the observational record but are a near-permanent feature of many climate and ocean simulations. A question not previously considered is the degree to which the Weddell polynya affects the nearby Filchner–Ronne Ice Shelf (FRIS) cavity. Here we assess these effects using regional ocean model simulations of the Weddell Sea and FRIS, where deep convection is imposed with varying area, location, and duration. In these simulations, the idealized Weddell polynyas consistently cause an increase in WDW transport onto the continental shelf as a result of density changes above the shelf break. This leads to saltier, denser source waters for the FRIS cavity, which then experiences stronger circulation and increased ice shelf basal melting. It takes approximately 14 years for melt rates to return to normal after the deep convection ceases. Weddell polynyas similar to those seen in observations have a modest impact on FRIS melt rates, which is within the range of simulated interannual variability. However, polynyas that are larger or closer to the shelf break, such as those seen in many ocean models, trigger a stronger response. These results suggest that ocean models with excessive Weddell Sea convection may not be suitable boundary conditions for regional models of the Antarctic continental shelf and ice shelf cavities.

1. Introduction

The Weddell Sea of Antarctica is weakly stratified, meaning that a small change in buoyancy forcing can trigger deep convection (Wilson et al. 2019). Furthermore, the deep waters of the Weddell Sea are warmer than the surface layers, as their density is dominated by salinity rather than temperature. Deep convection therefore causes the surface to warm, as Warm Deep Water (WDW) from below is mixed up into the colder, fresher mixed layer. As it is too warm to support sea ice cover, a region of open water forms within the ice pack: an open-ocean polynya, often termed the "Weddell polynya."

It is not known how often the Weddell polynya was present prior to the advent of satellite-based observations in the 1970s. Since then, it has occurred only rarely. The winters of 1974–76 displayed a Weddell polynya of area 2–3 $\times$ 10^5 km^2 (Carsey 1980). Hydrographic observations taken before and after the event showed that it caused a substantial cooling of the deep water, attributed to deep convection and the associated heat loss to the atmosphere (Gordon 1982). Following this event, the Weddell polynya more or less disappeared. Some years showed reduced springtime sea ice concentration in the region (Lindsay et al. 2004), particularly 1994 (Fetterrer et al. 2017), but a definite polynya did not occur again until 2017. This polynya was much smaller than before (0.3–0.35 $\times$ 10^5 km^2) and was only present for several months (Fetterrer et al. 2017; Jena et al. 2019). At the time of writing, it has not reappeared. It is possible that a long-term surface freshening is making deep convection in this region less likely (de Lavergne et al. 2014).

Despite the scarcity of the Weddell polynya in the observational record, it is a near-permanent feature of many ocean model simulations. Most coupled atmosphere–ocean models in phase 5 of the Coupled Model Intercomparison Project (CMIP5) simulate deep convection in the Weddell Sea, either permanently or periodically (de Lavergne et al. 2014; Heuzé et al. 2013). In some

Denotes content that is immediately available upon publication as open access.

Corresponding author: Kaitlin A. Naughten, kaight@bas.ac.uk

DOI: 10.1175/JCLI-D-19-0203.1

models this convection oscillates on a multicentennial time scale (Martin et al. 2013), switching on when sufficient heat has built up at middepth and switching off when this heat reservoir has been depleted. Stand-alone ocean/sea ice models with prescribed atmospheric forcing also commonly show permanent polynyas (Heuzé et al. 2015), unless special care is taken with vertical mixing schemes (Timmermann and Beckmann 2004) and/or the surface freshwater budget (Kjellsson et al. 2015). At the same time as they overestimate deep ocean convection, many ocean models struggle to form dense water on the Antarctic continental shelf (Heuzé et al. 2013). In other words, models tend to form Antarctic Bottom Water in the wrong regions and through the wrong processes. However, it is unclear whether the two opposing biases are related.

Although we have less than 50 years of observations, and it is possible that the Weddell polynya was more frequent prior to this time, it is clear that many ocean models are unrealistically susceptible to this phenomenon. The possible reasons for this widespread bias include insufficient freshwater input at the surface, possibly caused by an incomplete representation of ice-sheet–ocean interactions or a bias in net precipitation (Kjellsson et al. 2015; Marsland and Wolff 2001), as well as overly shallow summertime mixed layer depths (Timmermann and Beckmann 2004). In both cases, a positive salinity bias near the surface continues to grow until the water column becomes unstable and convects. This problem can be extremely stubborn (Goosse and Fichefet 2001; Heuzé et al. 2015; Dufour et al. 2017) and in many cases cannot be rectified without surface salinity restoring (Naughten et al. 2018) or freshwater hosing (Kjellsson et al. 2015). The impacts of excessive Weddell Sea convection on a simulation can be severe and typically include a strengthened Antarctic Circumpolar Current (Behrens et al. 2016), increased oceanic uptake of carbon (Bernardello et al. 2014), and large perturbations in Atlantic water mass properties. If such a prolonged, large-scale convection event were to happen in the real world, it would have major impacts on the climate.

The Weddell polynya is therefore of interest from an observational perspective, because of its recurrence in 2017, and also from a modeling perspective, because of the widespread tendency of models to overestimate its frequency. Despite an abundance of recent scientific discourse on the topic, one question has not been addressed: how does the Weddell polynya impact Antarctic ice shelves?

Ice shelves are the coastal margins of the Antarctic Ice Sheet that float on the ocean surface, forming ice shelf cavities beneath. These regions of ice-sheet–ocean interaction are key players for global sea level rise (Joughin and Alley 2011), as ice shelves buttress the land-based ice sheet and thereby restrain its flow. The Weddell Sea contains a number of ice shelves, but the largest is the Filchner–Ronne Ice Shelf (FRIS), which has been studied more than any other. The FRIS cavity has been the subject of field campaigns since the 1980s (Nicholls et al. 2009), and we therefore have a relatively good understanding of processes and conditions in the cavity, at least compared with other ice shelves. The circulation beneath FRIS has also been identified as a potential tipping point for ice shelf melting in the twenty-first century (Hellmer et al. 2012). Since FRIS is fed by multiple ice streams draining a large fraction of the Antarctic ice sheet, a reduction in its buttressing capability as a result of enhanced basal melting would have serious consequences for global sea level rise.

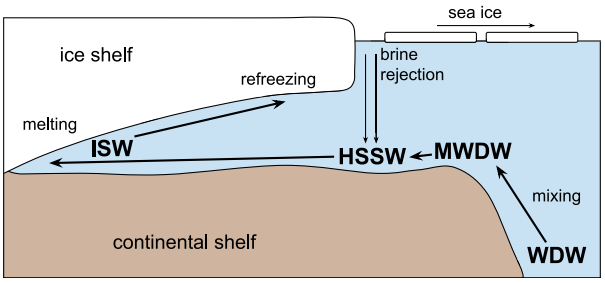

FIG. 1. Schematic of water mass transformations beneath the Filchner–Ronne Ice Shelf and surrounding continental shelf. WDW = Warm Deep Water, MWDW = Modified Warm Deep Water, HSSW = High Salinity Shelf Water, ISW = Ice Shelf Water.

A comprehensive review of processes beneath FRIS and on the surrounding continental shelf can be found in Nicholls et al. (2009); here we provide a brief summary to introduce the relevant water masses (see Fig. 1). This region of the continental shelf is largely fed by WDW (approximately 0.5°C) from the deep Weddell Sea, which upwells along surfaces of neutral buoyancy and crosses the continental shelf break. As it travels it mixes with cooler, fresher water masses, forming Modified Warm Deep Water (MWDW). Closer to the FRIS ice shelf front, strong sea ice formation transforms the water mass, setting it to the surface freezing point (approximately −1.9°C) and increasing its salinity through brine rejection. The result is termed High-Salinity Shelf Water (HSSW), which is the main water mass flowing into the FRIS cavity. The pressure dependence of the freezing point means that HSSW is warm enough to cause melting at the ice shelf base. It is then transformed to Ice Shelf Water (ISW), which is colder than the surface freezing point. If the ISW later travels to shallower depths where the in situ freezing point is higher, it becomes supercooled and refreezes on the ice

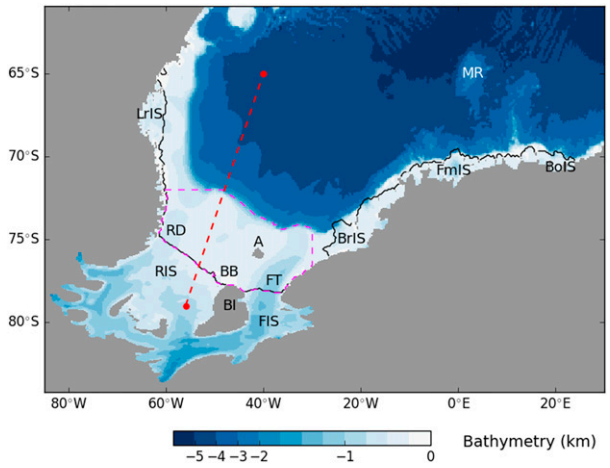

FIG. 2. Map of the model domain. The blue shading shows bathymetry (km); note the nonlinear color scale. Ice shelf fronts are contoured in black. The dashed red line is the transect shown in Fig. 6. The dashed magenta line outlines the continental shelf region analyzed in section 4d. Labels show locations mentioned in the text: RIS = Ronne Ice Shelf, FIS = Filchner Ice Shelf, RD = Ronne Depression, BB = Berkner Bank, BI = Berkner Island, FT = Filchner Trough, A = grounded iceberg A23-A, LrIS = Larsen Ice Shelf, BrIS = Brunt Ice Shelf, FmIS = Fimbul Ice Shelf, BoIS = Borchgrevink Ice Shelf, MR = Maud Rise. The text also uses the acronym EWIS, which includes BrIS, FmIS, BoIS, and the smaller ice shelves in between.

shelf base. Not shown in Fig. 1 is Antarctic Surface Water (AASW), a seasonal water mass occurring in ice-free areas during the summer. AASW is fresh and relatively warm, as a result of solar heating, and can cause strong seasonal melting of the ice shelf front.

2. Methods

a. Model description

Simulations are performed using the Massachusetts Institute of Technology general circulation model (MITgcm) (Marshall et al. 1997; Losch 2008), version 67d, with ocean, sea ice, and ice shelf components. This configuration uses a regional domain covering the Weddell Gyre and the continental shelves of the Weddell Sea. The domain is bounded by the Antarctic Peninsula to the west, the FRIS grounding line to the south, and open eastern and northern boundaries at 30°E and 61°S, respectively (Fig. 2). The Antarctic Peninsula has been extended slightly to the north so that the western boundary is completely closed. Horizontal grid spacing is 0.25° scaled by cosine of latitude, leading to Cartesian grid spacing ranging from 3 km in the south to 13 km in the north. In the vertical dimension, there are 120 levels with varying resolution: 10 m near the surface, 25 m for all depths covered by the FRIS cavity, and 100–350 m in the deep ocean. This configuration uses the z^* coordinate system, and also includes partial cells to allow a more accurate representation of topography.

Bathymetry and ice shelf draft are interpolated from the Bedmap2 dataset, with updated bathymetry in the Filchner cavity by Rosier et al. (2018). We also include the grounded iceberg A23-A, as represented in the RTopo-2 dataset (Schaffer et al. 2016), which is treated as land. Including this grounded iceberg in the model caused simulated circulation beneath FRIS to become more realistic [see Nøst and Østerhus (1998) for a discussion of its observed impact on sea ice formation].

The model is forced with the ERA-Interim atmospheric reanalysis (Dee et al. 2011) over the period 1979–2016, with 6-hourly fields for atmospheric state variables from which bulk fluxes are computed. An additional freshwater flux field representing iceberg melt is applied to the model as a monthly climatology, created using output of the NEMO G07 model (Storkey et al. 2018), which includes a statistical iceberg component.

Initial conditions for temperature and salinity are provided by the Southern Ocean State Estimate (SOSE) monthly climatology (Mazloff et al. 2010). Within ice shelf cavities, which are not included in SOSE, we impose constant initial conditions of −1.9°C and 34.4 psu. Initial velocities and sea surface height are set to zero. SOSE also provides open boundary conditions for temperature, salinity, and horizontal velocities. A sponge is applied to the open boundaries to ensure stability, whereby restoring to the boundary conditions occurs progressively over 8 grid cells. The restoring time scales on the inner and outer edges of the sponge are 1 year and 1 week, respectively. A small, constant correction is applied to the normal velocity at each boundary to offset nonzero net transport into the domain, which would otherwise lead to large changes in sea surface height. For the sea ice model, SOSE provides initial conditions for sea ice concentration and thickness, as well as boundary conditions for concentration, thickness, and ice velocities. No sponge is used for the sea ice boundary conditions. Instead, the normal ice velocity is smoothed over 3 grid cells to prevent sea ice convergence at the open boundaries.

This configuration uses the GM-Redi parameterization of geostrophic eddies (Gent and McWilliams 1990; Gent et al. 1995; Redi 1982), with background diffusion of $10\,m^2\,s^{-1}$ modified by the spatially varying coefficients of Visbeck et al. (1997). Vertical mixing is given by the K-profile parameterization (KPP) (Large et al. 1994). Tracer advection follows the third-order direct-space–time scheme with flux limiters. The sea ice model uses modified elastic–viscous–plastic dynamics (Lemieux et al. 2012; Bouillon et al. 2013; Kimmritz

et al. 2015) with 100 subcycles. There are seven ice thickness categories, but these are fictitious classes used for thermodynamics calculations only, and do not form a prognostic thickness distribution.

Ice shelf thermodynamics follows the standard three-equation parameterization (Hellmer and Olbers 1989; Holland and Jenkins 1999; Losch 2008). We use an ice shelf basal drag coefficient of 0.0097, which was determined empirically for the Ronne Ice Shelf by Jenkins et al. (2010). Heat and salt transfer coefficients are functions of the friction velocity at the ice shelf base, following Holland and Jenkins (1999). As this configuration is not coupled with an ice sheet model, ice shelf geometry is assumed to remain constant over time. Basal melting and freezing are treated as thermodynamic mass fluxes, which affect the temperature, salinity, and volume of the ocean, but not the ice shelf thickness.

We do not explicitly simulate tides in this configuration, because of their strict requirements on the model time step in MITgcm and the associated computational expense (by a factor of 24 in this case). Enhanced background vertical diffusivity and viscosity coefficients (10^{-5} and $10^{-4}\,m^2\,s^{-1}$, respectively) may partially mimic tidal mixing, but this is not spatially varying. Since tides have been shown to affect simulated melt rates and circulation patterns beneath FRIS (Makinson et al. 2011; Mueller et al. 2018), we performed a short (3 year) test simulation including tides, to understand the impact their absence may have on our results. Tidal amplitudes and phases from the Circum-Antarctic Tidal Simulation 2008a (CATS2008a) inverse tidal model (Padman et al. 2008) were prescribed at the open boundaries of our domain, and the background vertical mixing from the baseline simulation was removed. It was not computationally feasible to extend this simulation for longer than 3 years. Note that this is less than the simulated residence time of the FRIS cavity (see section 4d), so although the simulation was initialized from a spun-up nontidal state, the effects of tides on the cavity will not have converged.

b. Creating polynyas

To study the effects of open-ocean polynyas, we must be able to create them in the model, and to have control over their location, extent, and duration. Such control is achieved by imposing regions of full-depth convection. This idealized approach has been used by other modeling studies, such as Gelderloos et al. (2011) who imposed convection by modifying the temperature field offline and then allowing the model to recover. Since we do not want the polynyas to recover immediately, we instead impose convection by applying strong vertical mixing throughout the entire water column. This homogenizes temperature and salinity and causes polynyas to form without the explicit addition of heat or salt fluxes. We impose this convection every time step as part of the KPP routine, by setting the KPP boundary layer depth to the seafloor in the given region. The water column is then treated as unstable regardless of its buoyancy, and strong vertical mixing coefficients are applied. Following the KPP boundary layer scheme, these coefficients are highest in the middle of the water column (approximately $12\,m^2\,s^{-1}$ for vertical eddy viscosity and $30\,m^2\,s^{-1}$ for vertical diffusivity of temperature and salinity), with the depth-averaged values approximately half of the respective maxima.

TABLE 1. Summary of simulations performed. All simulations ran for the period 1979–2016. They were initialized from the end of a spinup also simulating the years 1979–2016, meaning this period was repeated once. The spinup was in turn initialized from the SOSE climatology. The locations of the polynyas are also shown in Fig. 4.

Name	Polynya
Baseline	None
Maud Rise	$2.6 \times 10^5\,km^2$ over Maud Rise
Near Shelf	$2.6 \times 10^5\,km^2$ near shelf break
Maud Rise Big	$6.2 \times 10^5\,km^2$ over Maud Rise
Maud Rise Small	$0.34 \times 10^5\,km^2$ over Maud Rise
Maud Rise 5y	As for Maud Rise, but switched off after 5 years

For simplicity, the polynyas imposed in our experiments are elliptical. Their locations and areas are chosen to mimic polynyas seen in the observational record or in CMIP5 output. Table 1 lists the simulations performed, which each cover the period 1979–2016, and are initialized from a 38-yr spinup covering the same period (i.e., the atmospheric forcing is repeated once). The first such experiment is a baseline simulation, which has no open-ocean polynyas or deep convection in the Weddell Sea. Five additional perturbation experiments impose polynyas using the method described above, throughout the entire simulation period 1979–2016 (their locations can be seen in Fig. 4). The Maud Rise experiment places a polynya at (0°, 65°S) with area $2.6 \times 10^5\,km^2$, which is similar to the polynya seen in satellite observations from 1974 to 1976 (Carsey 1980). Near Shelf has a polynya of the same size but shifted closer to the continental shelf break of the Southern Weddell Sea, at (30°W, 70°S), which is a common location for open-ocean convection in CMIP5 models (Sallée et al. 2013) although this has never been observed. We also vary the size of the Maud Rise polynya, with Maud Rise Big (area $6.2 \times 10^5\,km^2$) similar to strongly convective CMIP5 models (de Lavergne et al. 2014), and Maud

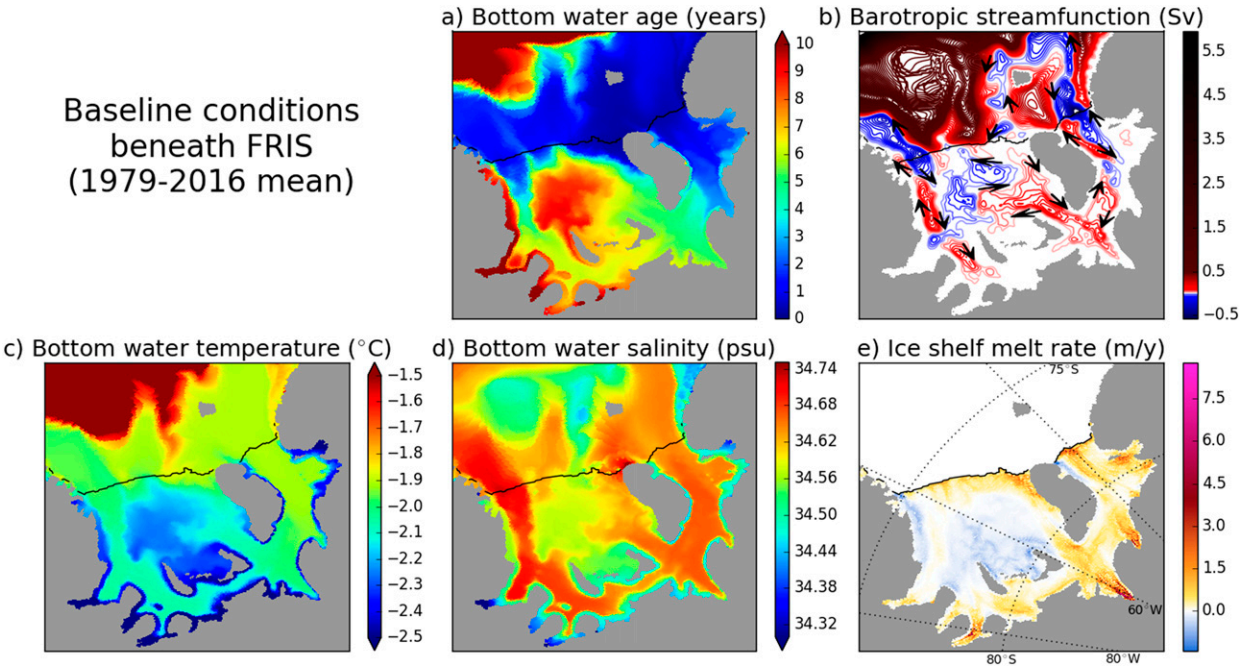

FIG. 3. Mean-state conditions beneath FRIS and on the surrounding continental shelf during the baseline simulation. Note the different projection to Fig. 1 (polar stereographic vs regular longitude–latitude). (a) Age tracer (years), which shows the amount of time since a water mass has been in contact with the atmosphere. Here we show the age tracer at the bottom of each water column. (b) Horizontal velocity streamfunction (Sv), vertically integrated through the water column. Contours are shown in intervals of 0.025 Sv. Positive cells (red) rotate clockwise and negative cells (blue) rotate counterclockwise, as indicated by the arrows. (c) Bottom water temperature (°C). (d) Bottom water salinity (psu). (e) Ice shelf melt rate (positive) or freezing rate (negative) (m yr^{-1}).

Rise Small (area $0.34 \times 10^5\,km^2$) similar to satellite observations in 2017 (Fetterrer et al. 2017). Finally, the Maud Rise 5y experiment imposes the same polynya as Maud Rise but switches it off after 5 years to investigate how long it takes the system to recover from open-ocean convection.

3. Assessment of baseline state

The mean state of the baseline simulation in the FRIS cavity and on the surrounding continental shelf is shown in Fig. 3. The age tracer (Fig. 3a) is strongly restored to zero at the sea surface and otherwise increases each time step. It therefore shows the amount of time since a given water mass was in contact with the atmosphere. In the bottom layer of the continental shelf, the highest values are in the northwest, where relatively old MWDW is transported across the shelf break. This transitions to much lower values throughout the rest of the continental shelf, revealing the strong ventilation of this region that results from sea ice formation. As the resulting HSSW flows along the seafloor and enters the cavity, its age increases, making the regions of inflow clearly apparent. The baseline simulation shows three main pathways of inflow, in agreement with observations (Nicholls et al. 2009): Ronne Depression, the western coast of Berkner Island, and Filchner Trough. However, the inflow into Filchner Trough is likely too strong compared with observations, suggesting that circulation is generally dominated by inflow west of Berkner Island, driving a net west-to-east flow around the island (Nicholls and Østerhus 2004; Nicholls and Johnson 2001). Nonetheless, observations in some years are dominated by Filchner Trough inflow, and the relative importance of these two circulation modes is not fully understood. The simulated inflow into the Ronne Depression also extends too far back into the cavity, as observations suggest that much of this inflow should cut across the central Ronne and join the inflow west of Berkner Island (Nicholls et al. 2009). However, transport of HSSW to the grounding lines of ice streams in the Ronne cavity is minimal, as indicated by relatively old bottom water in these regions.

The simulated horizontal velocity streamfunction (Fig. 3b) confirms the pathways of inflow suggested by Fig. 3a, and also reveals regions of outflow east of Berkner Island and on the western flank of Ronne Depression. These two regions of outflow agree with inferences made from observations. Refreezing has been observed on the western flank of Ronne Depression

(Nicholls et al. 2004), indicating that ISW flows out of the cavity here. Outflow east of Berkner Island agrees with the direction of flow inferred from CTD measurements in the cavity south of the island (Nicholls and Østerhus 2004) as well as ship-based measurements at the Filchner ice front (Darelius et al. 2014).

The Ronne cavity is mostly filled with ISW below the surface freezing point, which agrees with observations (Nicholls et al. 2009). Bottom water temperature (Fig. 3c) is too high in the Filchner cavity (Nicholls et al. 2009), likely a result of excessive inflow from the Filchner Trough that fills the cavity with water near the surface freezing point (approximately −1.9°C). Also note the tongues of MWDW (approximately −1.6°C) flowing onto the continental shelf outside the cavity, including one pathway reaching the Ronne Ice Shelf front around 53°W, which has been observed (Foldvik et al. 2001; Nicholls et al. 2008).

Bottom water salinity (Fig. 3d) reveals two main sources of HSSW, one in the Ronne Depression (34.71–34.73 psu) and one on Berkner Bank (34.7–34.75 psu). The locations of these maxima agree with observations (Nicholls et al. 2009), although the Ronne Depression HSSW is slightly too fresh and the Berkner Bank HSSW is slightly too salty. Since this bias in the salinity gradient persisted despite tuning of sea ice parameters, it is possible that it is ultimately caused by biases in the atmospheric forcing. In particular, the katabatic winds that drive sea ice formation are difficult for atmospheric reanalyses to properly resolve (Mathiot et al. 2010), and may therefore lead to inaccurate patterns of sea ice formation. It is also possible that biases in sea ice formation can explain the excessive Filchner Trough inflow in our simulations, which is driven by the Berkner Bank HSSW that recirculates into the cavity east of Berkner Island. If HSSW production were stronger in the Ronne Depression relative to Berkner Bank, we would expect a stronger inflow into the Ronne cavity to overpower the Filchner Trough inflow, and maintain west-to-east circulation around Berkner Island.

Patterns of basal melting and refreezing (Fig. 3e) are similar to observations (Moholdt et al. 2014; Rignot et al. 2013; Joughin and Padman 2003). The strongest melting occurs near the deep grounding lines of ice streams. More moderate melting is seen along the ice shelf front, on the western side of Berkner Island, and on the eastern flank of the Filchner Trough. Refreezing covers most of the interior Ronne Ice Shelf and is also present in the regions of ISW outflow along the east coast of Berkner Island and the western flank of the Ronne Depression. The only major disagreement with observed melt patterns is the relatively strong melting extending from the Filchner Ice Shelf front back along the Filchner Trough. This melting is due to excessive HSSW inflow into the Filchner Trough, as discussed above. The time-averaged basal mass loss from FRIS is 74 $\mathrm{Gt\,yr^{-1}}$ in this simulation, with a standard deviation of 8 $\mathrm{Gt\,yr^{-1}}$ in the annual averages. This result agrees with the observation-based estimates of Moholdt et al. (2014), Joughin and Padman (2003), and Depoorter et al. (2013), but is lower than the estimate of Rignot et al. (2013) (33% below the lower bound). The corresponding area-averaged melt rate is 0.19 $\mathrm{m\,yr^{-1}}$, which is slightly lower than the range of oceanographic estimates summarized by Nicholls et al. (2009) (5% below the lower bound).

The 3-yr simulation with tides (not shown) causes both melting and refreezing to increase beneath FRIS, because of the enhanced drag of tidal currents at the ice shelf base. Averaged over the last year of simulation, basal mass loss is 41% higher than in the baseline simulation. This value decreases over the 3-yr simulation, that is, net melt rates begin to converge toward the baseline, as the excess meltwater causes cooling within the cavity and therefore reduces the thermal driving. Indeed, water within the cavity is 0.05°C cooler and 0.02 psu fresher than the baseline, as a volume-average. Mean circulation patterns beneath FRIS are generally similar to the baseline. Inflow into the cavity slightly weakens in the Ronne Depression and west of Berkner Island, and slightly strengthens in Filchner Trough, meaning circulation around Berkner Island is slightly less realistic than before. Resolved eddy activity increases along the central Ronne Ice Shelf front, which indicates a greater exchange of water masses across the ice shelf front in this region. A new current also appears along the back of the Ronne Ice Shelf, traveling from west to east behind the ice rises.

4. Result of polynya experiments

a. Open-ocean response

As expected, imposing regions of deep convection causes open-ocean polynyas to form. Figure 4 shows sea ice concentration time-averaged over each simulation, with the regions of imposed convection outlined in white. Note that the polynyas tend to spread outside of these predefined boundaries, especially for Maud Rise Big (Fig. 4d) where the polynya extends toward the Near Shelf region in some years. This spreading primarily results from saline surface water advecting from the polynyas into surrounding regions, which then convect.

The gradual expansion of convection can be seen in Fig. 5a, which plots time series of convective area (where

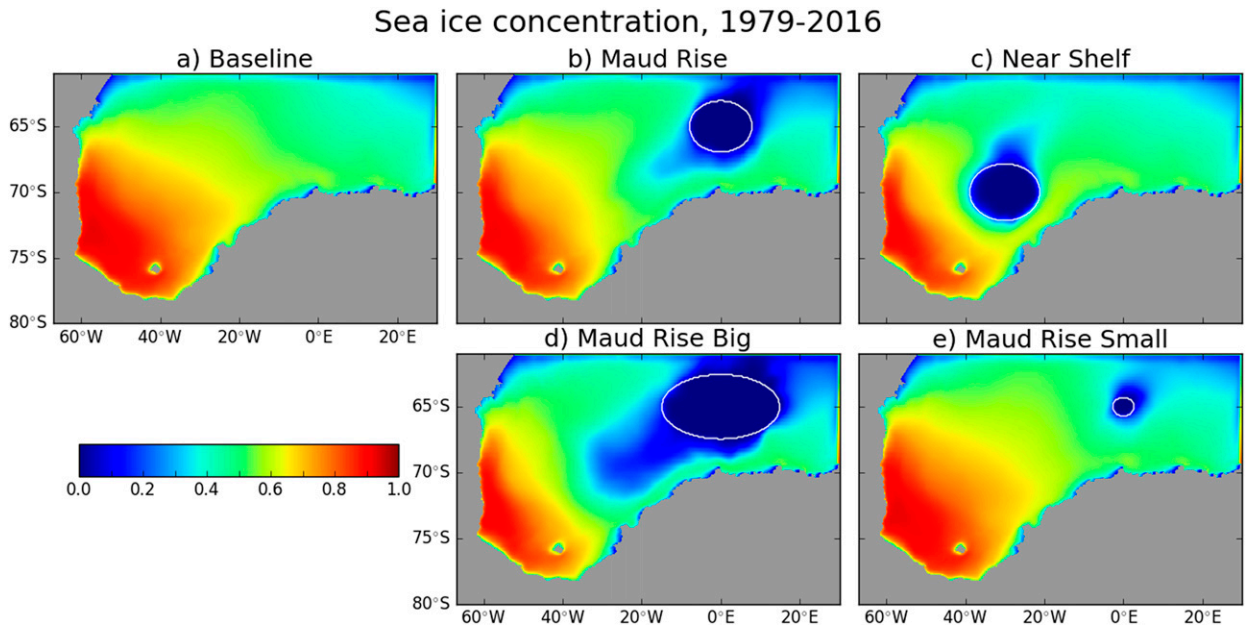

FIG. 4. Sea ice concentration time-averaged over each simulation. Regions of imposed deep convection are outlined in white.

the mixed layer depth exceeds 2000 m) for each simulation. Note that the expansion begins within the first year, meaning the initial values in Fig. 5a (annual averages over 1979) do not quite equal the imposed values given in Table 1. The Maud Rise Big convective area increases by 132% during the simulation (last year minus the imposed value), compared with the Maud Rise case, which increases by 88%, the Near Shelf case by 51%, and the Maud Rise Small case by 35%. We therefore find a positive feedback in Weddell Sea deep convection, which is stronger for larger polynyas. This concurs with the experiences of the authors using models that produce Weddell polynyas spontaneously (Naughten 2018). However, the convection is not unconditionally unstable, as convective area in the Maud Rise 5y case drops to zero within two years of the cessation of forced convection. Interannual variability also affects the convective area, as the level of stratification in regions surrounding the polynya is influenced by atmospheric forcing.

The convection causes cooling and freshening of deep waters (mainly WDW) within the polynya, and these signals spread throughout the basin. Depth-averaged through the center of the Maud Rise polynya, the

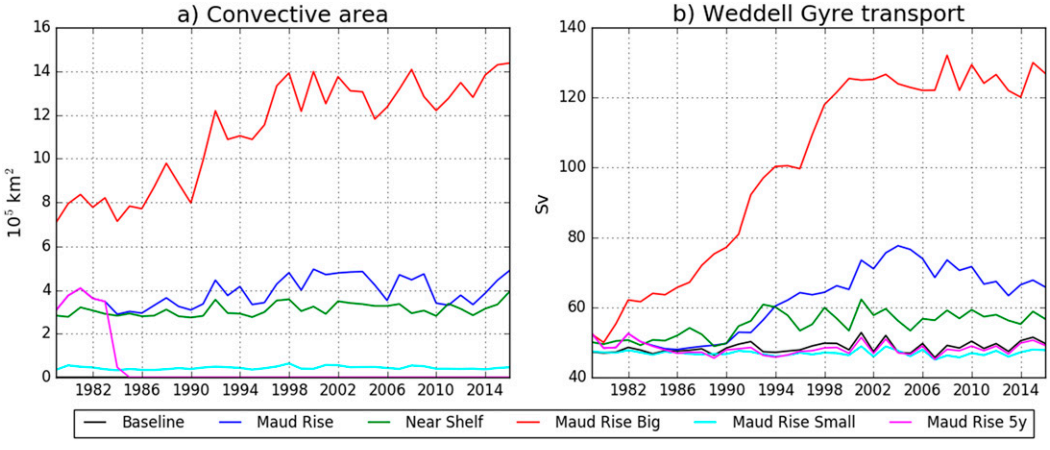

FIG. 5. Time series of annually averaged variables in each simulation. (a) Convective area (10^5 km^2), defined as the area with mixed layer depth exceeding 2000 m. (b) Weddell Gyre transport (Sv), defined as the absolute value of the minimum (most negative) barotropic transport streamfunction within the domain.

anomalies are −0.6°C and −0.04 psu (last year minus first year). Cooling of WDW occurs through two main processes: mixing of cold surface waters with the deep layers, and heat loss to the atmosphere. Note that these processes form a positive feedback, as mixing warms the surface and therefore increases its rate of heat loss. Freshening is mainly due to vertical mixing, with no positive feedback. There is also a small cooling and freshening effect from sea ice melting when the polynya first opens, but after the first year this is restricted to the margins of the polynya. Ultimately, the cooling of the WDW is strong enough to overpower the freshening, such that its density increases. This steepens the density gradient across the continental slope, causing the Antarctic Slope Current to speed up and therefore the Weddell Gyre to strengthen (Fig. 5b). The baseline Weddell Gyre transport averages 48 Sv (1 Sv ≡ $10^6\,m^3\,s^{-1}$), which is similar to estimates from data assimilation and inverse models (Mazloff et al. 2010; Sultan et al. 2007). This strengthens to 66 Sv in the Maud Rise case (average over last year), and 127 Sv in the Maud Rise Big case. The other simulations show a weaker response.

Cooling and freshening of WDW following convective events can also be seen in observations. Following the Weddell polynya of the 1970s, Gordon (1982) measured average anomalies of −0.2°C and −0.02 psu in the WDW mass, which strengthened to −0.4°C and −0.03 psu in the immediate vicinity of the polynya. These observations show a larger relative role of freshening than in our simulations, which may be influenced by atmospheric feedbacks that our model cannot capture, or by differences in the local sea ice properties. However, the observed WDW density anomaly is still positive. Observations also show warming of WDW in the decades following the 1970s polynya (Robertson et al. 2002), which is likely at least partially a result of recovery from the polynya, although it may also be influenced by the background warming trend of climate change. Cooling of WDW in the late 1990s has been attributed to the polynya-like reduction in sea ice concentration over Maud Rise in 1994 (Smedsrud 2005).

Despite the idealized nature of our simulated polynyas, we do not observe spurious behavior at their margins. While full-depth convection is imposed on certain grid cells, it is not limited to those cells, but rather is free to expand. By not imposing any conditions on the surrounding regions, we avoid a hard boundary around the polynya, which would be undesirable as it could lead to spurious currents. Velocities near the polynya region do become stronger, caused by density-driven changes in transport as noted above. The center of the Weddell Gyre also shifts toward the polynya, indicating stronger cyclonic transport around the polynya region.

b. Changes to onshore transport

While the imposed polynyas in our simulations cause cooling and freshening in the deep ocean, the opposite signal is seen on the continental shelf near FRIS. The MWDW mass on the continental shelf becomes warmer and saltier, as shown in Fig. 6.

The onshore transport of MWDW is clearly visible in the baseline simulation (left column of Fig. 6) as a tongue of relatively warm and salty water (approximately −0.8°C, 34.5 psu) extending onto the continental shelf from offshore. As this water mass travels south, strong sea ice formation extracts its heat and increases its salinity, producing HSSW that sinks to the bottom of the water column.

The Maud Rise experiment (center column of Fig. 6, with anomalies in the right column) shows a thicker, warmer, and saltier layer of MWDW crossing the shelf break. The positive salinity anomaly persists into the HSSW formation regions and into the cavity. However, the temperature of the HSSW is essentially unchanged, since the vertical mixing associated with sea ice formation sets it to the surface freezing point regardless of any temperature anomalies in the source water.

To understand why the onshore transport of MWDW increases, consider the density structure above the continental shelf break (Fig. 6c). A V-shaped depression in isopycnals illustrates the Antarctic Slope Front in this region (Thompson et al. 2018; Jacobs 1991; Gill 1973). Above the V is cold, relatively fresh winter water (WW), which is the year-round remnant of the deep winter mixed layer. In other regions of the Antarctic coastline, WW fills the entire continental shelf, and isopycnals slope monotonically downward above the shelf break. However, strong sea ice formation in the Weddell Sea forms dense HSSW on the shelf, raising isopycnals to the south and creating the V shape.

In our simulations, the main process transporting MWDW across the shelf break is eddy transport of heat and salt. Since eddies are mostly unresolved in our configuration, this process is parameterized by the GM-Redi scheme. Eddies act to flatten the steep isopycnals on the northward side of the V, between the WDW and the WW. This combines the two water masses, creating MWDW, which is carried onto the continental shelf. In the Maud Rise simulation, these isopycnals have become steeper, as the WDW is cooler and denser. Eddy transport across the isopycnals therefore increases, which is evident from a heat budget analysis (not shown). Even though the WDW core is cooler and fresher, the stronger transport means that it is less modified as it crosses the

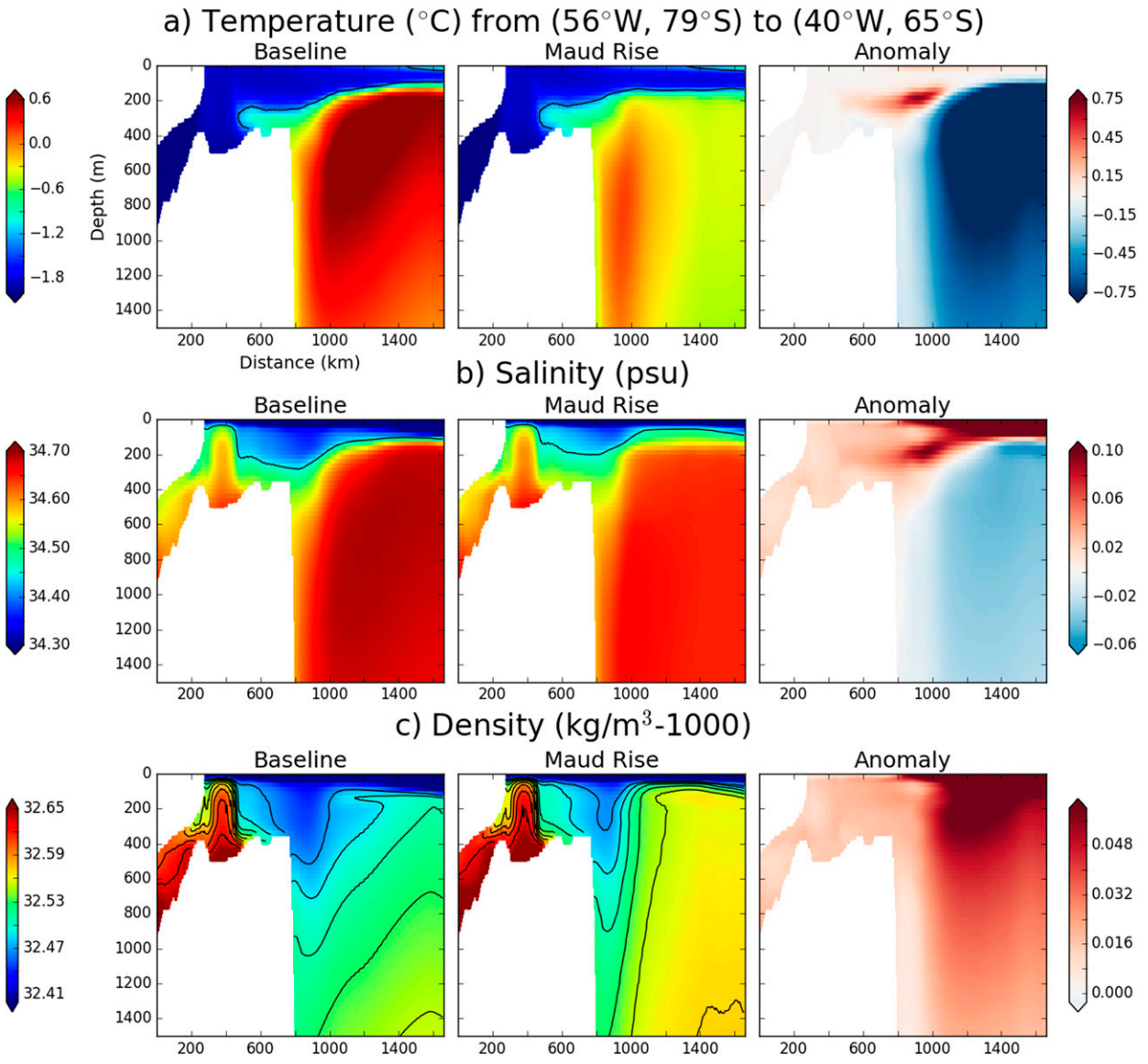

FIG. 6. Simulated conditions along a transect between 56°W, 79°S and 40°W, 65°S, which crosses the continental shelf in front of the Ronne Ice Shelf (visible in the top left corner of each plot). The transect line is shown in Fig. 2. All variables are averaged over the simulation period 1979–2016. (a) Temperature (°C). The −1.3°C isotherm is contoured in black. (b) Salinity (psu). The 34.45 isohaline is contoured in black. (c) Density, referenced to 1000-m depth (kg m^{-3} − 1000). The black contours show isopycnals from 32.47 to 32.65 kg m^{-3} in steps of 0.02 kg m^{-3}. The small zig-zags in some contours are artifacts of the transect plotting algorithm.

shelf break. The resulting MWDW crossing the shelf is therefore warmer and saltier.

All other simulations with imposed polynyas show similar behavior, to varying degrees. The mechanism is strongest in the Near Shelf and Maud Rise Big cases. In the former, the deep ocean cooling is concentrated most closely to the shelf break; in the latter, the deep ocean cooling has the greatest magnitude. In both cases, the raising of isopycnals within the WDW core is more pronounced than in the Maud Rise case. The Maud Rise Small simulation shows a slight, but still perceptible, response.

c. *Response of FRIS cavity*

Increased transport of warmer, saltier MWDW onto the continental shelf has consequences for the FRIS cavity. As shown in Fig. 7a, the temperature anomaly does not propagate into the cavity, because the extra heat is lost during sea ice formation over the continental shelf. However, warm anomalies on the continental

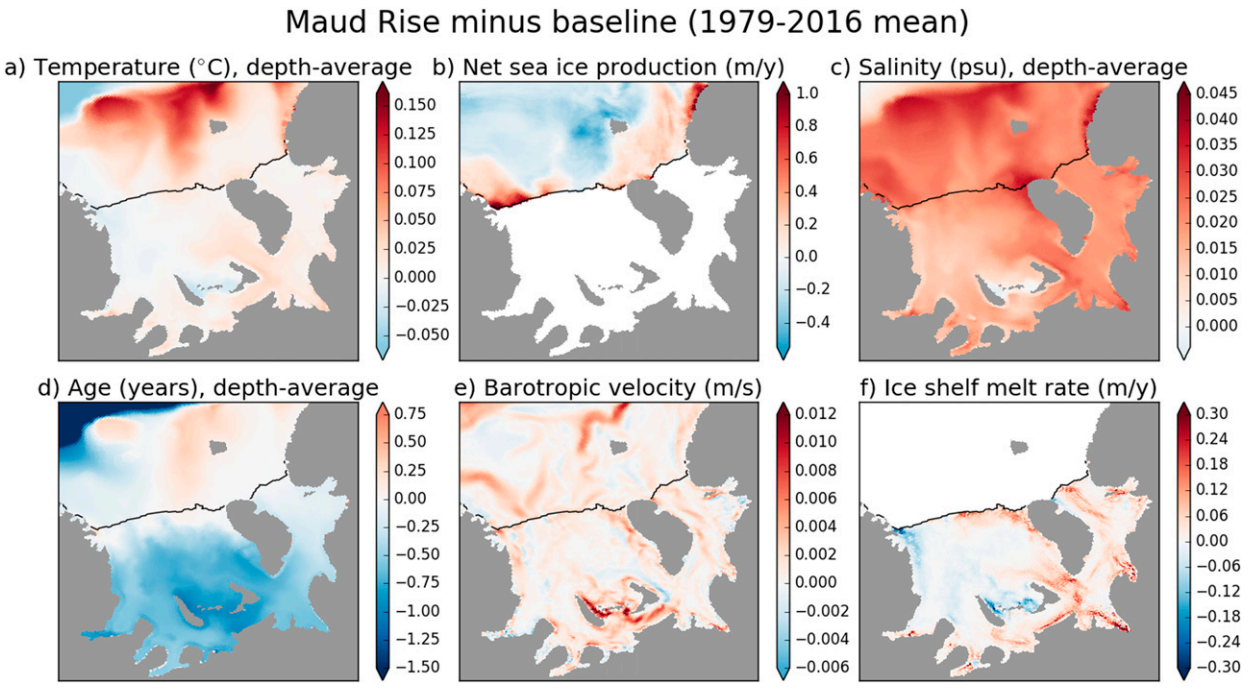

FIG. 7. Time-averaged anomalies in the FRIS cavity and on the surrounding continental shelf, for the Maud Rise simulation with respect to the baseline simulation. The anomalies shown in (e) refer to velocity magnitude.

shelf do cause the sea ice to thin. The thinner ice is weaker and more easily deformed, making it more mobile. Sea ice export from the continental shelf therefore increases, which exposes coastal regions to stronger atmospheric cooling. The net effect (Fig. 7b) is for sea ice production to decrease on the outer continental shelf (where melting dominates) and to increase along the ice shelf front (where freezing dominates).

Salinity increases throughout the continental shelf (Fig. 7c) as a result of the stronger MWDW transport. This is compounded by increased sea ice formation in HSSW production regions, such as Ronne Depression and Berkner Bank, where the salinification is particularly strong. The salinity anomalies relative to the baseline continue to grow over time, and do not stabilize during the 38-yr simulation. Since salinification of the cavity lags behind salinification of the continental shelf, an enhanced salinity gradient between the cavity and the continental shelf is maintained throughout the entire simulation. This leads to stronger buoyancy-driven circulation that flushes the cavity more rapidly, decreasing its residence time. Indeed, the age tracer within the cavity (Fig. 7d) decreases by an average of 0.5 years as a result of the Maud Rise polynya. As implied by the shorter residence time, barotropic currents within the cavity are stronger (Fig. 7e).

Since HSSW entering the FRIS cavity is at the surface freezing point by definition, any changes in temperature within the cavity must be a result of changes in residence time. Faster flushing of the cavity means that the heat fluxes of ice shelf melting, which cause cooling of the source water, are spread out over a larger volume of HSSW. However, this faster flushing also increases the rate of melting, and therefore the magnitude of the heat fluxes. In this case, the net effect of the shorter residence time is to cause slight warming in most of the cavity (Fig. 7a).

Comparing the anomalies in ice shelf basal melt rates (Fig. 7f) to the baseline melt rates (Fig. 3e), it generally holds that regions of melting become more positive and regions of freezing become more negative. That is, the stronger circulation causes an amplification of the existing melt/freeze pattern. On balance, basal mass loss from FRIS increases. Note that biases in the existing pattern, namely, the excessive melting in the Filchner Trough (see section 3), are also amplified. The relatively strong increases in central Filchner melt rates should therefore be treated with caution.

All of these changes are quite consistent between the different polynya simulations, varying only in magnitude. One way to compare the different magnitudes is with time series of net basal mass loss from FRIS (Fig. 8a). Compared with the baseline simulation, the Maud Rise polynya causes FRIS mass loss to increase by between 5% and 15%. Since the standard deviation in baseline melt rates is 11%, this response is within the

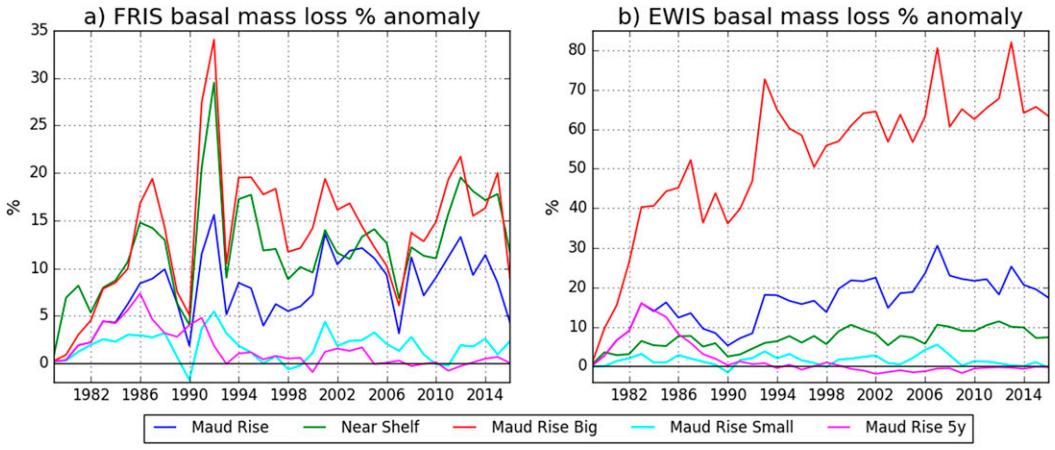

FIG. 8. Time series of annually averaged ice shelf basal mass loss for each simulation, expressed as a percentage change from the baseline time series. (a) Filchner–Ronne Ice Shelf; (b) eastern Weddell ice shelves.

range of interannual variability. However, the Near Shelf and Maud Rise Big cases both show a larger response (up to 30%), as a result of stronger density changes near the shelf break as described in section 4b. For the Maud Rise Small polynya, increases in mass loss do not exceed 5%. In each simulation, the anomalies are concentrated in the winter months (not shown), confirming that the increased melt results from stronger pulses of dense HSSW. Also note that the effects of atmospheric forcing variability on melt rates (such as the maximum in 1992) are not quite linear, and therefore are not completely removed by subtracting the baseline. That is, the strongest anomalies in melt rates correspond to years that already have the strongest melt.

The model domain also includes the eastern Weddell ice shelves (EWIS), from the Brunt Ice Shelf in the west (approximately 28°W) to the Borchgrevink Ice Shelf in the east (approximately 20°E) (see Fig. 2). Their time-averaged basal mass loss in the baseline simulation is 74 Gt yr^{-1}, which agrees with the observational estimates of Rignot et al. (2013). In the polynya simulations, basal mass loss from these ice shelves (Fig. 8b) shows an even greater response than FRIS, with increases of up to 30% for the Maud Rise simulation. In comparison, the Near Shelf simulation shows a weaker response (up to 10%), as the polynya is farther away. The Maud Rise Big polynya drives increases of up to 80%, and the Maud Rise Small polynya of up to 5%.

The mechanism causing increased melting beneath the EWIS is simpler than for FRIS. Sea ice formation is much weaker on the Eastern Weddell continental shelf, so MWDW can flow directly into some cavities (such as the Fimbul Ice Shelf) without first being transformed to HSSW (see also Hattermann et al. 2014). Warm anomalies in MWDW are therefore preserved, and propagate into the cavities, causing increased melting through thermal driving alone.

d. Recovery time

The Maud Rise 5y experiment is identical to Maud Rise for the first 5 years. After this time, the imposed polynya is removed and the simulation continues as per the baseline experiment. Section 4a noted that the deep convection itself shuts down relatively quickly, with convective area dropping to zero within two years. How long does it take for the FRIS cavity to recover from the polynya, and to return to baseline conditions?

Answering this question is complicated by the relatively large interannual variability in conditions beneath FRIS. However, this variability is mostly driven by the atmospheric forcing, which is common to all simulations. Also note that the ice shelf–ocean–sea ice system is chaotic and will never return to exactly the same conditions as in the baseline experiment. Nonetheless, at some point the anomalies will become small enough to be considered background noise, and the long-term averages will converge.

For a given time series variable, such as basal mass loss from FRIS, we use a signal-to-noise approach to estimate the point at which the Maud Rise 5y time series is no longer significantly different from the baseline time series. First, we subtract the baseline from Maud Rise 5y, to remove the interannual variability common to both simulations. We also annually average the time series to remove the seasonal cycle. Then we calculate the signal-to-noise ratio

$$S(t) = \frac{\mu_5(t)}{\sigma_5(t)} \tag{1}$$

for each year t, starting in 1984 (the year the polynya is switched off). Here $\mu_5(t)$ and $\sigma_5(t)$ are the mean and

standard deviation over the 5-yr period centered at year t. We consider the variable to have "recovered" at the first value of t for which $|S(t)| < 1$. Note this is a somewhat arbitrary threshold, as the anomaly time series gradually converges to zero.

Using this method, FRIS basal mass loss recovers in 1998. There are individual years before this time with near-zero anomalies (e.g., 1993, see Fig. 8a) but it is not until 1998 that a 5-yr period has no significant anomaly. This is 14 years after the imposed polynya is removed, meaning that FRIS melt rates feel the effects of the polynya for almost 4 times as long as the polynya is actually open. For comparison, the average residence time of the FRIS cavity (i.e., the volume-averaged age tracer in the cavity) varies between 4 and 7 years in the baseline simulation, and is slightly shorter throughout the Maud Rise 5y simulation. This means that the slow recovery of melt rates cannot be explained simply by the time it takes to flush the cavity once. Rather, there are further delays due to the recovery of MWDW and HSSW properties on the continental shelf.

To investigate this process, we volume-average temperature and salinity over the continental shelf in front of FRIS, defined by the bounds 62°–30°W, 79°–72°S and the 1250-m isobath, as marked in Fig. 2. Salinity recovers in 2000 (i.e., in 16 years), but is extremely close to the threshold $|S(t)| = 1$ in 1994 (10 years) and every following year. It is therefore likely that the density gradients along the pathways of inflow into the cavity, which determine the rate of flushing of the cavity and therefore the melt rates, recover at some point during the period 1994–2000. Indeed, the volume-averaged age tracer beneath FRIS recovers in 1997 (13 years), which nearly coincides with the recovery of the melt rates.

Temperature on the continental shelf shows a more complex response: the warm anomalies recover in 1998, but then overshoot and become slightly cooler than the baseline conditions until 2013. This overshoot indicates that the cooling in the deep ocean is finally reflected on the continental shelf. As the density structure above the shelf break returns to baseline conditions (i.e., the isopycnals flatten), transport of MWDW across the shelf break also returns to normal. However, the WDW core is still cooler than in the baseline simulation, and this temperature signal is then reflected in the MWDW.

It is likely that the recovery time depends on the duration of convection, as polynyas that are open for longer cause more modification of deep water masses. Also note that the recovery of the deep ocean in our simulations is greatly aided by restoring at the open boundaries. In reality, it would take much longer for WDW properties to return to their preconvective state. Our estimates of recovery time should therefore be considered lower bounds.

5. Discussion

The Weddell polynyas imposed in our experiments are clearly idealized. In reality, convection may occur on a seasonal basis rather than year-round, and may not be full-depth. Polynyas are also likely to move around slightly from year to year, as seen in the 1970s (Carsey 1980). Furthermore, our model domain is regional, and the deep ocean is restored to a weakly stratified state at the open lateral boundaries. This restoring may explain why the baseline simulation does not produce Weddell polynyas spontaneously, the way many other ocean/sea ice models do. Restoring is also likely to help the deep ocean recover more quickly once imposed convection is switched off.

The polynyas in our simulations are held open for the entire 38-yr period, which is much longer than any convective event in the observational record. However, this time scale is not unusual for ocean models, many of which exhibit permanent or multidecadal polynyas. Our experiments are therefore best suited to assess the impact of this widespread model bias. It is still possible to interpret our results from a more observational perspective, by only considering the first few years of each simulation. Note that the Maud Rise 5y experiment suggested that the FRIS cavity continues to be affected by Weddell polynyas even after they close, in this case for more than a decade.

While our baseline simulation generally agrees with observations in the FRIS region, some biases persist in sea ice formation, which affects circulation and water mass properties beneath the ice shelf. Our simulations also do not resolve tides, which according to our tests would increase net basal melting from FRIS and result in a slightly cooler, fresher cavity. While these limitations impact the baseline state of the model, we do not expect them to substantially affect the model's response to Weddell polynyas, as the processes we have outlined here do not depend on any specific details of sub–ice shelf circulation or cavity water masses. Perhaps a more important shortcoming is the lack of a coupled atmosphere in our simulations, which means that atmospheric feedbacks with the polynya are not considered. It is possible that such feedbacks could affect the degree of cooling and/or freshening of WDW within the polynya, and these processes should be the focus of future research.

Nonetheless, our simulations provide important insights into the FRIS cavity's response to Weddell polynyas. While all polynya scenarios show a measurable

response in our experiments, this response would be more difficult to detect in observations, where there is no control case for comparison. Observational uncertainty, which is particularly large for basal melt rates (Rignot et al. 2013; Depoorter et al. 2013), also makes trends more difficult to detect. With this in mind, the 2017 Weddell polynya was likely too small to cause perceptible changes in the observed FRIS region. The cavity's response to the 1970s Weddell polynya, represented by our Maud Rise experiment, may have also been within the range of interannual variability. However, the stronger response of the Maud Rise Big and Near Shelf experiments raises concerns, as these polynyas resemble those seen in many ocean models.

It is already known that ocean models that convect too often and too strongly in the Weddell Sea are likely to exhibit a cold and fresh bias in WDW, a strengthened Weddell Gyre, and (in global or circumpolar models) increased transport of the Antarctic Circumpolar Current (Heuzé et al. 2015). Our simulations suggest that such models can also be expected to show biases on the Antarctic continental shelf and in ice shelf cavities. In particular, the MWDW flux across the continental shelf break of the Weddell Sea is likely to be too strong. If ice shelf cavities are resolved by the model, circulation and melt rates beneath FRIS will increase as a result.

Historically, global coupled models have not included ice shelf cavities, and have barely resolved the continental shelf. However, this is changing as high resolution becomes more affordable and the importance of studying ice–ocean interactions becomes widely recognized (Storkey et al. 2018) (G. Marques 2019, personal communication). It may be tempting for ice shelf–ocean modelers to treat excessive Weddell polynya activity as a far-field bias that does not affect the cavities. Unfortunately, our simulations suggest that this bias cannot be safely ignored.

6. Conclusions

We have presented a new Weddell Sea configuration of MITgcm, which exhibits reasonable agreement with observations in the FRIS cavity and on the surrounding continental shelf. By imposing regions of full-depth convection, we simulate the effects of Weddell polynyas on the continental shelf and the FRIS cavity. The most significant consequence is an increase in WDW transport onto the continental shelf, as a result of changes in density structure over the shelf break. Increasing salinity on the continental shelf then flushes the FRIS cavity more rapidly and increases its melt rates. We find that this process is more sensitive to Weddell polynyas that are larger and/or closer to the shelf break. Even after open-ocean convection ceases, basal melt rates take more than a decade to recover, reflecting lags in WDW transport and the residence time of the FRIS cavity. Future work should include coupled atmosphere models and full tidal forcing to investigate their impact on the results.

If and when the Weddell polynya reappears in observations, its impact on FRIS and the continental shelf might be difficult to detect, given sparse measurements and interannual variability. Regardless, our results suggest that ice shelf–ocean modelers should exercise caution with configurations showing excessive open-ocean convection, and should endeavor to address this bias wherever possible.

Acknowledgments. We thank Ralph Timmermann and Hartmut Hellmer for helpful discussions while tuning the model, Ryan Patmore for advice on the Weddell Gyre domain, and Maria Vittoria Guarino for advice on statistical analysis of the recovery time. Finally, Ralph Timmermann and two anonymous reviewers provided helpful comments on an earlier version of this manuscript. This research is part of the Filchner Ice Shelf System (FISS) project NE/L013770/1. David Munday is also supported by the ORCHESTRA project NE/N018095/1. Computational resources were provided by the ARCHER U.K. National Supercomputing Service.

REFERENCES

Behrens, E., G. Rickard, O. Morgenstern, T. Martin, A. Osprey, and M. Joshi, 2016: Southern Ocean deep convection in global climate models: A driver for variability of subpolar gyres and Drake Passage transport on decadal timescales. *J. Geophys. Res. Oceans*, **121**, 3905–3925, https://doi.org/10.1002/2015JC011286.

Bernardello, R., I. Marinov, J. B. Palter, E. D. Galbraith, and J. L. Sarmiento, 2014: Impact of Weddell Sea deep convection on natural and anthropogenic carbon in a climate model. *Geophys. Res. Lett.*, **41**, 7262–7269, https://doi.org/10.1002/2014GL061313.

Bouillon, S., T. Fichefet, V. Legat, and G. Madec, 2013: The elastic-viscous-plastic method revisited. *Ocean Modell.*, **71**, 2–12, https://doi.org/10.1016/j.ocemod.2013.05.013.

Carsey, F. D., 1980: Microwave observation of the Weddell polynya. *Mon. Wea. Rev.*, **108**, 2032–2044, https://doi.org/10.1175/1520-0493(1980)108<2032:MOOTWP>2.0.CO;2.

Darelius, E., K. Makinson, K. Daae, I. Fer, P. R. Holland, and K. W. Nicholls, 2014: Hydrography and circulation in the Filchner Depression, Weddell Sea, Antarctica. *J. Geophys. Res. Oceans*, **119**, 5797–5814, https://doi.org/10.1002/2014JC010225.

Dee, D. P., and Coauthors, 2011: The ERA-Interim reanalysis: Configuration and performance of the data assimilation system. *Quart. J. Roy. Meteor. Soc.*, **137**, 553–597, https://doi.org/10.1002/qj.828.

de Lavergne, C., J. B. Palter, E. D. Galbraith, R. Bernardello, and I. Marinov, 2014: Cessation of deep convection in the open Southern Ocean under anthropogenic climate change. *Nat. Climate Change*, **4**, 278–282, https://doi.org/10.1038/nclimate2132.

Depoorter, M. A., J. L. Bamber, J. A. Griggs, J. T. M. Lenaerts, S. R. M. Ligtenberg, M. R. van den Broeke, and G. Moholdt, 2013: Calving fluxes and basal melt rates of Antarctic ice shelves. *Nature*, **502**, 89–92, https://doi.org/10.1038/nature12567.

Dufour, C. O., A. K. Morrison, S. M. Griffies, I. Frenger, H. Zanowski, and M. Winton, 2017: Preconditioning of the Weddell Sea polynya by the ocean mesoscale and dense water overflows. *J. Climate*, **30**, 7719–7737, https://doi.org/10.1175/JCLI-D-16-0586.1.

Fetterrer, F., K. Knowles, W. Meier, M. Savoie, and A. K. Windnagel, 2017: Sea Ice Index, version 3. NSIDC, Boulder, CO, accessed 21 January 2019, https://doi.org/10.7265/N5K072F8.

Foldvik, A., T. Gammelsrød, E. Nygaard, and S. Østerhus, 2001: Current measurements near Ronne Ice Shelf: Implications for circulation and melting. *J. Geophys. Res.*, **106**, 4463–4477, https://doi.org/10.1029/2000JC000217.

Gelderloos, R., C. A. Katsman, and S. S. Drijfhout, 2011: Assessing the roles of three eddy types in restratifying the Labrador Sea after deep convection. *J. Phys. Oceanogr.*, **41**, 2102–2119, https://doi.org/10.1175/JPO-D-11-054.1.

Gent, P. R., and J. C. McWilliams, 1990: Isopycnal mixing in ocean circulation models. *J. Phys. Oceanogr.*, **20**, 150–155, https://doi.org/10.1175/1520-0485(1990)020<0150:IMIOCM>2.0.CO;2.

——, J. Willebrand, T. J. McDougall, and J. C. McWilliams, 1995: Parameterizing eddy-induced tracer transports in ocean circulation models. *J. Phys. Oceanogr.*, **25**, 463–474, https://doi.org/10.1175/1520-0485(1995)025<0463:PEITTI>2.0.CO;2.

Gill, A. E., 1973: Circulation and bottom water production in the Weddell Sea. *Deep-Sea Res.*, **20**, 111–140, https://doi.org/10.1016/0011-7471(73)90048-x.

Goosse, H., and T. Fichefet, 2001: Open-ocean convection and polynya formation in a large-scale ice-ocean model. *Tellus*, **53A**, 94–111, https://doi.org/10.3402/tellusa.v53i1.12175.

Gordon, A. L., 1982: Weddell deep water variability. *J. Mar. Res.*, **40**, 199–217, https://doi.org/10.1093/icesjms/40.2.199.

Hattermann, T., L. H. Smedsrud, O. A. Nøst, J. M. Lilly, and B. K. Galton-Fenzi, 2014: Eddy-resolving simulations of the Fimbul Ice Shelf cavity circulation: Basal melting and exchange with open ocean. *Ocean Modell.*, **82**, 28–44, https://doi.org/10.1016/j.ocemod.2014.07.004.

Hellmer, H. H., and D. J. Olbers, 1989: A two-dimensional model for the thermohaline circulation under an ice shelf. *Antarct. Sci.*, **1**, 325–336, https://doi.org/10.1017/S0954102089000490.

——, F. Kauker, R. Timmermann, J. Determann, and J. G. L. Rae, 2012: Twenty-first-century warming of a large Antarctic ice-shelf cavity by a redirected coastal current. *Nature*, **485**, 225–228, https://doi.org/10.1038/nature11064.

Heuzé, C., K. J. Heywood, D. P. Stevens, and J. K. Ridley, 2013: Southern Ocean bottom water characteristics in CMIP5 models. *Geophys. Res. Lett.*, **40**, 1409–1414, https://doi.org/10.1002/grl.50287.

——, J. K. Ridley, D. Calvert, D. P. Stevens, and K. J. Heywood, 2015: Increasing vertical mixing to reduce Southern Ocean deep convection in NEMO3.4. *Geosci. Model Dev.*, **8**, 3119–3130, https://doi.org/10.5194/gmd-8-3119-2015.

Holland, D. M., and A. Jenkins, 1999: Modeling thermodynamic ice–ocean interactions at the base of an ice shelf. *J. Phys. Oceanogr.*, **29**, 1787–1800, https://doi.org/10.1175/1520-0485(1999)029<1787:MTIOIA>2.0.CO;2.

Jacobs, S. S., 1991: On the nature and significance of the Antarctic Slope Front. *Mar. Chem.*, **35**, 9–24, https://doi.org/10.1016/S0304-4203(09)90005-6.

Jena, B., M. Ravichandran, and J. Turner, 2019: Recent reoccurrence of large open ocean polynya on the Maud Rise seamount. *Geophys. Res. Lett.*, **46**, 4320–4329, https://doi.org/10.1029/2018GL081482.

Jenkins, A., K. W. Nicholls, and H. F. J. Corr, 2010: Observation and parameterization of ablation at the base of Ronne Ice Shelf, Antarctica. *J. Phys. Oceanogr.*, **40**, 2298–2312, https://doi.org/10.1175/2010JPO4317.1.

Joughin, I., and L. Padman, 2003: Melting and freezing beneath Filchner-Ronne Ice Shelf, Antarctica. *Geophys. Res. Lett.*, **30**, 1477, https://doi.org/10.1029/2003GL016941.

——, and R. B. Alley, 2011: Stability of the West Antarctic ice sheet in a warming world. *Nat. Geosci.*, **4**, 506–513, https://doi.org/10.1038/ngeo1194.

Kimmritz, M., S. Danilov, and M. Losch, 2015: On the convergence of the modified elastic-viscous-plastic method for solving the sea ice momentum equation. *J. Comput. Phys.*, **296**, 90–100, https://doi.org/10.1016/j.jcp.2015.04.051.

Kjellsson, J., and Coauthors, 2015: Model sensitivity of the Weddell and Ross Seas, Antarctica, to vertical mixing and freshwater forcing. *Ocean Modell.*, **94**, 141–152, https://doi.org/10.1016/j.ocemod.2015.08.003.

Large, W. G., J. C. McWilliams, and S. C. Doney, 1994: Oceanic vertical mixing—A review and a model with a nonlocal boundary-layer parameterization. *Rev. Geophys.*, **32**, 363–403, https://doi.org/10.1029/94RG01872.

Lemieux, J. F., D. A. Knoll, B. Tremblay, D. M. Holland, and M. Losch, 2012: A comparison of the Jacobian-free Newton-Krylov method and the EVP model for solving the sea ice momentum equation with a viscous-plastic formulation: A serial algorithm study. *J. Comput. Phys.*, **231**, 5926–5944, https://doi.org/10.1016/j.jcp.2012.05.024.

Lindsay, R. W., D. M. Holland, and R. A. Woodgate, 2004: Halo of low ice concentration observed over the Maud Rise seamount. *Geophys. Res. Lett.*, **31**, L13302, https://doi.org/10.1029/2004GL019831.

Losch, M., 2008: Modeling ice shelf cavities in a z coordinate ocean general circulation model. *J. Geophys. Res.*, **113**, C08043, https://doi.org/10.1029/2007JC004368.

Makinson, K., P. R. Holland, A. Jenkins, K. W. Nicholls, and D. M. Holland, 2011: Influence of tides on melting and freezing beneath Filchner-Ronne Ice Shelf, Antarctica. *Geophys. Res. Lett.*, **38**, L06601, https://doi.org/10.1029/2010GL046462.

Marshall, J., C. Hill, L. Perelman, and A. Adcroft, 1997: Hydrostatic, quasi-hydrostatic, and nonhydrostatic ocean modeling. *J. Geophys. Res.*, **102**, 5733–5752, https://doi.org/10.1029/96JC02776.

Marsland, S. J., and J.-O. Wolff, 2001: On the sensitivity of Southern Ocean sea ice to the surface freshwater flux: A model study. *J. Geophys. Res.*, **106**, 2723–2741, https://doi.org/10.1029/2000JC900086.

Martin, T., W. Park, and M. Latif, 2013: Multi-centennial variability controlled by Southern Ocean convection in the Kiel Climate Model. *Climate Dyn.*, **40**, 2005–2022, https://doi.org/10.1007/s00382-012-1586-7.

Mathiot, P., B. Barnier, H. Gallée, J. M. Molines, J. L. Sommer, M. Juza, and T. Penduff, 2010: Introducing katabatic winds in global ERA40 fields to simulate their impacts on the Southern Ocean and sea-ice. *Ocean Modell.*, **35**, 146–160, https://doi.org/10.1016/j.ocemod.2010.07.001.

Mazloff, M. R., P. Heimbach, and C. Wunsch, 2010: An eddy-permitting Southern Ocean state estimate. *J. Phys. Oceanogr.*, **40**, 880–899, https://doi.org/10.1175/2009JPO4236.1.

Moholdt, G., L. Padman, and H. A. Fricker, 2014: Basal mass budget of Ross and Filchner-Ronne ice shelves, Antarctica, derived from Lagrangian analysis of ICESat altimetry. *J. Geophys. Res. Earth Surf.*, **119**, 2361–2380, https://doi.org/10.1002/2014JF003171.

Mueller, R. D., T. Hattermann, S. L. Howard, and L. Padman, 2018: Tidal influences on a future evolution of the Filchner-Ronne Ice Shelf cavity in the Weddell Sea, Antarctica. *Cryosphere*, **12**, 453–476, https://doi.org/10.5194/tc-12-453-2018.

Naughten, K. A., 2018: Modelling Antarctic ice shelf, ocean, and sea ice interactions under present-day and future climate scenarios. Ph.D. thesis, University of New South Wales, 200 pp.

——, K. J. Meissner, B. K. Galton-Fenzi, M. H. England, R. Timmermann, H. H. Hellmer, T. Hattermann, and J. B. Debernard, 2018: Intercomparison of Antarctic ice-shelf, ocean, and sea-ice interactions simulated by MetROMS-iceshelf and FESOM 1.4. *Geosci. Model Dev.*, **11**, 1257–1292, https://doi.org/10.5194/gmd-11-1257-2018.

Nicholls, K. W., and M. R. Johnson, 2001: Oceanographic conditions south of Berkner Island, beneath Filchner-Ronne Ice Shelf, Antarctica. *J. Geophys. Res.*, **106**, 11 481–11 492, https://doi.org/10.1029/2000JC000350.

——, and S. Østerhus, 2004: Interannual variability and ventilation timescales in the ocean cavity beneath Filchner-Ronne Ice Shelf, Antarctica. *J. Geophys. Res.*, **109**, C04014, https://doi.org/10.1029/2003JC002149.

——, K. Makinson, and S. Østerhus, 2004: Circulation and water masses beneath the northern Ronne Ice Shelf, Antarctica. *J. Geophys. Res.*, **109**, C12017, https://doi.org/10.1029/2004JC002302.

——, L. Boehme, M. Biuw, and M. A. Fedak, 2008: Wintertime ocean conditions over the southern Weddell Sea continental shelf, Antarctica. *Geophys. Res. Lett.*, **35**, L21605, https://doi.org/10.1029/2008GL035742.

——, S. Østerhus, K. Makinson, T. Gammelsrød, and E. Fahrbach, 2009: Ice-ocean processes over the continental shelf of the southern Weddell Sea, Antarctica: A review. *Rev. Geophys.*, **47**, 1–23, https://doi.org/10.1029/2007RG000250.

Nøst, O. A., and S. Østerhus, 1998: Impact of grounded icebergs on the hydrographic conditions near the Filchner Ice Shelf. *Ocean, Ice and Atmosphere: Interactions at the Antarctic Continental Margin*, S. S. Jacobs, and R. F. Weiss, Eds., Antarctic Research Series, Vol. 75, Amer. Geophys. Union, 267–284, https://doi.org/10.1029/AR075p0267.

Padman, L., S. Y. Erofeeva, H. A. Fricker, and S. L. Howard, 2008: CATS2008a_opt: Circum-Antarctic Tidal Simulation, Inverse Model Version 2008a. Earth & Space Research, accessed 18 September 2018, https://www.esr.org/research/polar-tide-models/list-of-polar-tide-models/cats2008/.

Redi, M. H., 1982: Oceanic isopycnal mixing by coordinate rotation. *J. Phys. Oceanogr.*, **12**, 1154–1158, https://doi.org/10.1175/1520-0485(1982)012<1154:OIMBCR>2.0.CO;2.

Rignot, E. J., S. S. Jacobs, J. Mouginot, and B. Scheuchl, 2013: Ice-shelf melting around Antarctica. *Science*, **341**, 266–270, https://doi.org/10.1126/science.1235798.

Robertson, R., M. Visbeck, A. L. Gordon, and E. Fahrbach, 2002: Long-term temperature trends in the deep waters of the Weddell Sea. *Deep-Sea Res. II*, **49**, 4791–4806, https://doi.org/10.1016/S0967-0645(02)00159-5.

Rosier, S. H. R., and Coauthors, 2018: A new bathymetry for the southeastern Filchner-Ronne Ice Shelf: Implications for modern oceanographic processes and glacial history. *J. Geophys. Res. Oceans*, **123**, 4610–4623, https://doi.org/10.1029/2018JC013982.

Sallée, J.-B., E. Shuckburgh, N. Bruneau, A. J. S. Meijers, T. J. Bracegirdle, and Z. Wang, 2013: Assessment of Southern Ocean mixed-layer depths in CMIP5 models: Historical bias and forcing response. *J. Geophys. Res. Oceans*, **118**, 1845–1862, https://doi.org/10.1002/jgrc.20157.

Schaffer, J., R. Timmermann, J. E. Arndt, S. S. Kristensen, and C. Mayer, 2016: A global, high-resolution data set of ice sheet topography, cavity geometry, and ocean bathymetry. *Earth Syst. Sci. Data*, **8**, 543–557, https://doi.org/10.5194/essd-8-543-2016.

Smedsrud, L. H., 2005: Warming of the deep water in the Weddell Sea along the Greenwich meridian: 1977–2001. *Deep-Sea Res. I*, **52**, 241–258, https://doi.org/10.1016/j.dsr.2004.10.004.

Storkey, D., and Coauthors, 2018: UK Global Ocean GO6 and GO7: A traceable hierarchy of model resolutions. *Geosci. Model Dev.*, **11**, 3187–3213, https://doi.org/10.5194/gmd-11-3187-2018.

Sultan, E., H. Mercier, and R. T. Pollard, 2007: An inverse model of the large scale circulation in the South Indian Ocean. *Prog. Oceanogr.*, **74**, 71–94, https://doi.org/10.1016/j.pocean.2007.02.001.

Thompson, A. F., A. L. Stewart, P. Spence, and K. J. Heywood, 2018: The Antarctic slope current in a changing climate. *Rev. Geophys.*, **56**, 741–770, https://doi.org/10.1029/2018RG000624.

Timmermann, R., and A. Beckmann, 2004: Parameterization of vertical mixing in the Weddell Sea. *Ocean Modell.*, **6**, 83–100, https://doi.org/10.1016/S1463-5003(02)00061-6.

Visbeck, M., J. Marshall, T. Haine, and M. Spall, 1997: Specification of eddy transfer coefficients in coarse-resolution ocean circulation models. *J. Phys. Oceanogr.*, **27**, 381–402, https://doi.org/10.1175/1520-0485(1997)027<0381:SOETCI>2.0.CO;2.

Wilson, E. A., S. C. Riser, E. C. Campbell, and A. P. S. Wong, 2019: Winter upper-ocean stability and ice–ocean feedbacks in the sea-ice-covered Southern Ocean. *J. Phys. Oceanogr.*, **49**, 1099–1117, https://doi.org/10.1175/JPO-D-18-0184.1.